Draft version June 23, 2004
Preprint typeset using LATEX style emulateapj v. 11/12/01

THE HOT SPOTS OF CYGNUS A AT 230 GHZ

M.C.H. Wright[1] and M. Birkinshaw[2]
Draft version June 23, 2004

ABSTRACT

We have imaged Cygnus A at 230 GHz with $\sim 1''$ angular resolution using the BIMA array. The hot spots have structures similar to those seen in images at 87, 15 and 5 GHz, but are more compact and show spectral index gradients indicating local synchrotron aging of the radiating electron population. Bright 230-GHz features, and the flattest spectra, are seen in and near compact hot spots B and E. There are no marked spectral breaks above 5 GHz for the hot spot spectra as a whole, so that relativistic electrons with energies $\gtrsim 10$ GeV are injected into both the compact and the extended hot spots on time scales less than 50,000 years. The X-ray emission of the hot spots, as measured by *Chandra*, more closely resembles the 5 GHz than the 230 GHz radio structures, as expected from an inverse-Compton interpretation of the X-ray emission. However, hot spots A and B are over-bright in X-rays relative to their 230-GHz emission. This may reflect a different magnetic field and electron population than in hot spot D.

Subject headings: galaxies: individual (Cygnus A) — radio continuum: galaxies — techniques: interferometric

1. INTRODUCTION

Cygnus A is the closest example of a powerful double radio galaxy. It is identified with a cD galaxy at $z = 0.0561$ (Owen et al. 1997), giving an angular scale of 1.09 $\mathrm{kpc\,arcsec^{-1}}$ ($H_0 = 70\ \mathrm{km\,s^{-1}\,Mpc^{-1}}$, $\Omega_\mathrm{m} = 0.3$, $\Omega_\Lambda = 0.7$). Cygnus A has been extensively imaged at frequencies from 150 MHz to 100 GHz with interferometer arrays providing $15''$ or better angular resolution. At low frequencies the predominantly double structure of the source is apparent in the symmetrical-looking radio lobes, while images at high resolution from 1.4 to 15 GHz reveal a complex structure, with two kpc-sized hot spots at the head of each 60-kpc radio lobe, and spectral gradients that correspond to synchrotron aging of the high energy electrons in the radio lobes as they flow back from the hot spots towards the center of the source (Carilli et al. 1991).

The expansion of a population of relativistic electrons generated in the nucleus during its passage to the hot spots within the jet will cause severe adiabatic losses. Furthermore, the $\sim 50,000$ year synchrotron radiative lifetime of electrons that radiate at 230 GHz (if the jet's magnetic field is similar to the hot spot field), is less than the light travel time from the nucleus. Thus unless the jet flow is relativistic (at $\gtrsim 0.9c$), and the expansion of the jet is slight, the radiation from the hot spots is the product of electrons accelerated locally, presumably as a result of the working of the jet at its termination. The relationship between the pairs of hot spots within each lobe is not clear in this model. If the hot spots represent working surfaces from different phases in the orientation of the jet, then we might expect them to show different spectral signatures, but no spectral breaks are apparent in the existing radio data. If they are separate features produced by a single jet, then we might also expect different spectra corresponding to different particle acceleration. High resolution images of the hot spots over the widest possible range of frequencies, which should reveal the sites of particle acceleration, might therefore help diagnose the physics of the pairs of hot spots. Comparison with X-ray images (Wilson, Young & Shopbell 2000) should show the relative location of concentrated fields and electrons, and measure the hot spot magnetic fields, with some remaining uncertainty caused by the dynamics of the flow (Tregillis, Jones & Ryu 2002).

In this paper we present $1''$ resolution imaging of Cygnus A at 230 GHz obtained with the BIMA array[3] and use our results to look for radio spectral effects in the hot spots that might arise from electron energy losses. We make comparisons with the *Chandra* X-ray data to test the spectral models used for magnetic field measurement and the inverse-Compton origin of the X-ray emission.

2. OBSERVATIONS

Observations were obtained between 2000 Nov and 2001 Jan using 9 antennas from the BIMA array (Welch et al., 1996). Cygnus A was observed using three configurations of the antennas providing 72 antenna separations from 6.3 to 240 m. Observations were made in left circular polarization at 230 GHz to avoid sensitivity to linear polarization, and in linear polarization at 215 GHz where no quarter wave plates were available to convert to circular polarization. We observed three pointings centered on the nucleus and the hot spots. The data were sampled at 36 s intervals, interleaved so that each pointing center was observed at 108 s intervals. The quasar 2007+404 was observed as a phase calibrator at 25 min intervals. The strong quasar 3C 454.3 was observed as a bandpass calibrator during the times that Cygnus A transits, since Cygnus A is then so close to the zenith that the antennas slew rapidly in azimuth and the pointing errors are large. Pointing offsets were determined from observations of 2007+404 at 90 GHz.

[1] Radio Astronomy Lab, University of California, Berkeley, CA 94720
[2] Department of Physics, University of Bristol, Bristol BS8 1TL, UK
[3] The BIMA array is operated by the Berkeley-Illinois-Maryland Association under funding from the National Science Foundation

The data were calibrated and imaged using the MIRIAD software package (Wright and Sault, 1993; Sault, Teuben and Wright, 1995). The instrumental phase was calibrated from the 2007+404 observations. The antenna gains were determined from observations of planets at short antenna separations. The three pointings were imaged separately since the primary beam FWHM $\sim 50''$, is less than half the separation of the pairs of hot spots at the ends of the lobes, and the emission from the extended radio lobes is weak at 230 GHz. Each sideband of the local oscillator was used to image the data in an 800 MHz band at 215 and 230 GHz. These 4 sets of images, at each of the 3 pointings, were consistent with an RMS noise 4-7 mJy derived from the observed system temperatures, which ranged from 600 to 1200 K. Although the original intent had been to combine the 215 and 230 GHz observations in a multifrequency synthesis (MFS) to improve the *uv* coverage, the linear polarized 215 GHz observations were of lower quality and were rejected for the sake of polarization purity. The lower and upper sideband images at 230 GHz were combined in an MFS image with a mean frequency 228.6 GHz, and deconvolved using the CLEAN algorithm. Uniform weighting of the data results in a synthesized beam FWHM of $0.98'' \times 0.86''$ with an RMS noise level of 7 mJy/beam. Robust weighting gives a beam FWHM $1.65'' \times 1.38''$ with an RMS noise level of 4 mJy/beam.

3. RESULTS

The 230 GHz images are shown in Figures 1 and 2 superposed on VLA images at 5 and 15 GHz (Carilli, private communication) convolved to the same resolution. At 230 GHz, hot spots A and B in the Np lobe coincide with their counterparts at 5 and 15 GHz, while the peaks of hot spots D and E in the Sf lobe are displaced slightly from their positions seen at 5 and 15 GHz.

We computed spectral index distributions by comparing the hot spot images at 5 and 15 GHz from the VLA and 87 GHz from BIMA (Wright, Chernin and Forster 1997) with the new 230 GHz images, all convolved to the same ($0.98'' \times 0.86''$) resolution. The 230 GHz images are remarkably similar to those at 5, 15 and 87 GHz. We used the `MIRIAD` task `IMDIFF`, which finds optimum parameters in a maximum likelihood sense, to compare the 230 GHz images with those at the other frequencies. The parameters used were an amplitude scale factor, an amplitude offset, and shifts in x and y direction. The 230 GHz images agree with the 5, 15 and 87 GHz images within ± 2 times the RMS noise level of 7 mJy/beam, and small overall shifts in RA and DEC which are consistent with expectations based on the limited SNR and image fidelity at 230 and 87 GHz.

The `IMDIFF` results allow us to derive average spectral indices (α, defined in the sense that the flux density at frequency ν, $S_\nu \propto \nu^{-\alpha}$) for the emission within the hot spot regions shown in Figures 1 and 2. The overall $5-230$ GHz spectral index $\alpha_5^{230} = 1.13$ for hot spots A and B, and 1.06 for hot spots D and E. Using the same technique, the average $5-15$ GHz spectral index, $\alpha_5^{15} = 1.13$ for hot spots A and B, and 0.98 for hot spots D and E. The $15-230$ GHz spectral index, $\alpha_{15}^{230} = 1.13$ for hot spots A and B, and 1.14 for hot spots D and E. The $87-230$ GHz spectral index, $\alpha_{87}^{230} = 1.23$ for hot spots A and B, and 1.16 for hot spots D and E.

The absolute errors in these spectral index estimates are determined primarily by the flux density scale at each frequency. At 87 and 230 GHz, the flux density scale is tied to planetary observations, and flux density measurements at different observatories are typically consistent at the 10% level. The BIMA images obtained from the lower and upper sidebands, which are separated in frequency by 3 GHz, were independently calibrated and their calibration is good to within 10%. However, we estimate that the amplitude and phase errors in the data from atmospheric fluctuations raise the overall error in the 87 and 230 GHz flux densities to 12%. These errors lead to absolute errors ± 0.20 in α_5^{15}, ± 0.18 in α_{87}^{230}, and ± 0.04 in α_5^{230}.

The relative calibration between the hot spots does not depend on the absolute flux density scale, but only on the SNR and image fidelity (which is primarily determined by residual atmospheric phase errors at 87 and 230 GHz). Figure 3 shows the integrated spectra of the hot spot regions and the core of Cygnus A based on the 5, 15, 87, and 230 GHz data, for box-shaped regions which include both the compact hot spot and some more extended emission near each feature, since at our angular resolution these emissions cannot be cleanly separated. The errors on the flux densities plotted in Fig. 3 are the absolute errors discussed above. We conclude that the average high frequency spectral index α_{87}^{230} is not significantly steeper than α_5^{15} for any of the hot spots.

In Figures 1 and 2 we plot contours as a percentage of the peaks at 5, 15 and 230 GHz. Differences between the contours indicate spectral index variations across the images. This is most evident in the tails of hot spots A and B, which become progressively shorter from 5 to 230 GHz. The 12.5% contour is 12 mJy/beam ($1.7\times$ RMS) at 230 GHz. Emission extending over a few beam areas at 1.7 times the noise level is highly significant. With the limited signal-to-noise ratio (SNR) and image fidelity at 230 and 87 GHz we cannot make reliable spectral index images at $0.98'' \times 0.86''$ resolution since the error in the spectral index in each resolution element is large compared with the spectral index variations across the hot spots. We must use measures which integrate over several beam areas, or use images at more than one frequency, in order to obtain significant results.

Although the best fitting difference between the images is only an *average* ± 2 times the RMS noise level of 7 mJy/beam at 230 GHz at $0.98'' \times 0.86''$ resolution, there are significant difference between the images at 5, 15, 87 and 230 GHz which cannot be explained by noise or systematic errors in the data. The BIMA and VLA images are well sampled for structures on the $1-20$ arcsec scale of the hot spots. The observations of the hot spots and nucleus are interleaved, so that the unresolved nucleus serves as a good phase calibrator only ~ 1 arcmin from the hot spots, and observed at ~ 2 min intervals. Residual atmospheric phase fluctuations were calibrated using the nucleus as a secondary phase calibrator averaged over 5 minute intervals. The astrometry of the images is within $0.1''$ relative to the nucleus with an assumed position (J2000) RA = 19:59:28.348, DEC = 40:44:02.006. As a test, we made 230 GHz images shifted by $\pm 0.1''$ in RA and $\pm 0.1''$ in

DEC to see if the differences between the images could be attributed to position shifts. We found that the observed spectral index variations are not produced by, and their appearance is not consistent with, a simple rotation or shift of the images.

Figures 4 and 5 show contours at 5, 87 and 230 GHz superposed on an image of the spectral index between 5 and 15 GHz, α_5^{15}. In Figure 4, the 87 and 230 GHz emission follow the flatter α_5^{15} spectral index in the extended regions to the east and south of hot spot A. In Figure 5, hot spot spot E is twice as bright (2 contours) at 87 and 230 GHz relative to the the 5 GHz peak. Hot spot E has the flattest α_5^{15} spectral index.

In order to investigate these apparent spectral index variations across the images, we made images at four different resolutions using different weightings of the uv-data. Uniform weighting of the data results in a synthesized beam FWHM of $0.98'' \times 0.86''$ with an RMS noise level of 7 mJy/beam. The best SNR is obtained using natural weighting which gives a synthesized beam FWHM $2.52'' \times 2.09''$ and RMS thermal noise 3 mJy/beam. The best compromise between resolution and sensitivity for displaying spectral index images at 230 GHz is robust weighting, with a beam FWHM $1.65'' \times 1.38''$ and RMS noise level of 4 mJy/beam.

Figures 6 and 7 show contours at 5 and 230 GHz superposed on an image of the spectral index between 5 and 230 GHz, α_5^{230}. All images are shown at $1.65'' \times 1.38''$ resolution. The α_5^{230} spectral index images show a similar pattern to the α_5^{15} images. The peaks of hot spot A and B at 230 GHz are offset from those at 5 GHz towards the flatter spectral index. The peak in hot spot D is offset to the west of the peak at 5 GHz. The flattest spectral index is seen in hot spot E, which is offset to the south of the peak at 5 GHz.

The error in α_5^{230} is less than ± 0.1 at this resolution, and the 230-GHz images are consistent with the spectral index variations from 5 to 15 GHz shown in Figures 4 and 5. We see spectral index variations across all components, with the flattest index $\alpha_5^{230} = 0.8 \pm 0.1$ in compact hot spot E, and spectral index gradients ~ 0.1 arcsec^{-1} in A and D. These gradients are in good agreement with those previously seen between 5 and 15 GHz at 0.4 arcsec resolution (Carilli 1989) and between 8 and 43 GHz at 0.25 arcsec resolution (Carilli et al. 1999).

Although the image fidelity is limited at 230 GHz by atmospheric phase fluctuations and decorrelation, the data are well calibrated and it is not easy to produce systematic errors which would mimic the observed spectral index variations. The *uv* data were obtained at 3 epochs with east-west, north-south and diagonal interferometer baselines at each epoch. The *uv* data sampling is robust to systematic diurnal, calibration, and atmospheric errors. The main result of residual errors is to broaden the instrumental point spread function as seen in the measured width of the nucleus discussed below. In the higher resolution images the hot spots are resolved, and detailed spectral index variations are observed across the hot spots. A flatter spectral index, α_5^{15} and α_8^{43}, is observed on the south edge of hot spot E, to the west of D, to the north-east of A, and in the leading edge of hot spot B. At our $\sim 1''$ resolution these spectral index variations result in the offsets of the peaks that we see at 87 and 230 GHz.

Compact components B and E are extended along the jet axis and the more extended components A and D are resolved transverse to the jet axis. Similar structures are seen at 5, 15, and 87 GHz. A Gaussian fitting procedure applied to the hot spots at $0.98'' \times 0.86''$ resolution gives component locations at 5, 15, 87, and 230 GHz consistent to within $0.1''$. Fitted and deconvolved angular sizes for the hot spots are given in Table 1. While the SNR is lower at 87 and 230 GHz, the Gaussian fits reported in Table 1 clearly show that the hot spots become more compact from 5 to 230 GHz. This trend is not seen in the nucleus, which has a similar SNR. The errors in the Gaussian fits depend on the SNR and on the atmospheric decorrelation at 87 and 230 GHz. The radio flux densities have a $\sim$ 10% calibration error, and the errors in the FWHM for hot spots A, B and D were empirically measured to be $0.01 - 0.02''$ at 5 and 15 GHz, and $0.04 - 0.10''$ at 87 and 230 GHz. The width of hot spot E is poorly determined (with an error $\sim 0.5''$ at 230 GHz). The deconvolved size of the nucleus is significant because of residual calibration and atmospheric phase errors and the resulting decorrelations which are largest at 230 GHz. The FWHM values in Table 1 are not corrected for this instrumental and atmospheric "seeing". The clear conclusion from our results is that the hot spots are more extended at lower frequencies because of spectral index gradients.

4. DISCUSSION

4.1. *Spatial and spectral structure*

The 230 GHz data are consistent with no spectral break between 5 and 230 GHz for any of the detected hot spots at $1''$ resolution. The lack of a spectral break implies a continued injection of relativistic electrons on time scales less than the synchrotron loss timescale at the highest energy. Taking the field in the hot spots as being about half the equipartition field (Sec. 4.2), this indicates that electrons with energies ~ 10 GeV, generated in acceleration regions in the hot spots and radiating at 230 GHz, travel a few kpc in less than 50,000 years, and so either have streaming speeds $\gtrsim 0.1c$ or are subject to continuing reacceleration while within the hot spot regions.

If we assume that the electrons being continuously injected into the hot spots have the canonical $E^{-\delta}$ energy spectrum with $\delta = 2$, then the radio spectral index that we would expect is $\alpha = 0.5$ up to some frequency corresponding to a break energy, $E_{\rm break}$, above which the spectrum should steepen to $\alpha = 1$ (corresponding to $\delta = 3$), with a higher-frequency cutoff associated with the maximum electron energy, $E_{\rm max}$. Hot spots A and B display spectra steeper than $\alpha = 1$ without a cut-off. We model their electron spectra as a power law with a break by $\Delta\delta \sim 1.2$ at $E_{\rm break} \sim 1$ GeV, corresponding to a radiated frequency below 5 GHz. By contrast, the spectrum of hot spot D is consistent with a $\Delta\delta = 1$ break at low energy, and shows a spectral index $\alpha \approx 1$ over the entire radio to mm-wave spectrum. We interpret this difference as indicating that proportionately less spectrally-aged material is radiating in hot spot D than in hot spots A and B.

The radio spectral indices of diffuse emission in the lobes of Cygnus A are significantly higher than the values measured in the hot spots, but no additional information is available from our 230-GHz images since the lobes are resolved out. However, evidence of size changes in the hot spots, and spectral index gradients from the centres to the edges of the hot spot complexes, suggests that strong spectral ageing occurs as the electrons leave the hot spots and enter the lobes, except in a few special regions such as the tail features on hot spots B and E (e.g., Carilli, 1989). We cannot distinguish, however, the possibility that these regions are, instead, sites of additional acceleration to high energies caused by interactions with the jet flow.

4.2. *Comparison with the Chandra X-ray image*

Wilson et al. (2000) have used the *Chandra* satellite in comparison with radio data to show that the prominent X-ray emission from the hot spots of Cygnus A (Harris, Carilli and Perley 1994) arises from the inverse-Compton process in fields about half the strength predicted from equipartition/minimum energy arguments. We have recalculated the field strengths in the well-detected X-ray hot spots, A, B and D, using the same techniques, but with the spectral breaks $\Delta\delta$ required to fit the radio spectra. We also find values rather lower than the equipartition fields, and consistent with the values measured by Wilson et al. (Table 2). In this table, results are shown both for the canonical Galactic absorbing column towards Cygnus A ($N_{\rm H} = 3.06 \times 10^{21}$ cm^{-2}), and with an additional intrinsic column which we find to be required to fit the X-ray spectra, but which has only a small effect on the inferred magnetic fields.

It should be noted that the X-ray spectral indices are relatively flat compared with the radio spectral indices. This is explained, on our spectral model, by the presence of the break in the electron spectrum at $E_{\rm break} \sim 1$ GeV. This induces a gentle curvature in the X-ray spectrum and causes the effective X-ray spectral (energy) index, $\alpha_{\rm x}$, to be slightly above 0.5. The absence of a cut-off in the radio to mm-wave hot spot spectra indicates that the maximum electron energy $E_{\rm max} \gtrsim 10$ GeV. However, the absence of IR emission from the hot spots implies that the electron spectrum must have $E_{\rm max} \lesssim 100$ GeV (Carilli et al. 1999). Detailed spectral work, with improved mm-wave resolution and deeper IR and X-ray data, will allow the electron energy spectrum to be determined at several locations within the hot spots, and so will provide new information on transport and loss processes.

The magnetic fields that we measure in the hot spots imply that the electrons which are responsible for upscattering radio photons to X-ray energies (and so have energies of about 10 GeV) themselves radiate synchrotron radiation at $\sim$ 10 GHz, and so the angular sizes of the hot spots at X-ray energies should more closely resemble the angular size at low radio frequencies than the smaller angular sizes that we measure at 87 and 230 GHz. Such a correspondance is seen in Table 1: the best-fit Gaussian angular sizes of the hot spots decrease from 5 to 230 GHz but increase in the X-ray. This angular structure test provides additional confirmation that the emission process in the radio knots is synchrotron self-Compton radiation, where the electron population scatters its own radio emission. Inverse-Compton scattering of the external radiation field to X-ray energies should be unimportant in these hot spots, unless the electron fluid moves relativistically (with Lorentz factor $\gtrsim 3$). Such fast motions cannot be ruled out based on our data, but higher resolution images of the structures of the hot spots at multiple radio frequencies should test simple models of this type.

In Figures 8 and 9 we compare the *Chandra* 0.5 - 8.0 keV X-ray and radio images. In order to register the X-ray and radio images it was necessary to shift the X-ray data by $\sim 1''$ with a small field rotation. All images are convolved to $(0.98'' \times 0.86'')$ resolution. A detailed comparison of these images reveals some interesting differences. Hot spots A and B are the most over-bright in X-rays relative to their 230-GHz emission (in the sense that the total X-ray counts that they produce are high relative to their total 230-GHz flux densities), although the difference from hot spot D is less than a factor of 1.5. Our favoured interpretation is that A and B are currently in a transient phase of their evolution, where they show a particularly high X-ray output. Such phases are found in MHD simulations, such as those of Tregillis et al. (2002), and add an extra uncertainty in the calculation of the magnetic fields of hot spots from X-ray and radio maps. We might speculate that similar high X-ray outputs might be common in other radio sources with multiple hot spots (e.g., in 3C 351; Hardcastle et al. 2003). For hot spot D, the X-ray emission clearly extends beyond the 230-GHz hot spot, with the tail being particularly bright.

If we assume that the X-rays arise from inverse-Compton emission, while the radio emission is produced by the synchrotron process then, recalling that the radio and X-ray emission originate from electrons with similar energies, the differences between the X-ray and radio images are attributable to different ratios of magnetic field and radiation energy densities in the hot spots. Thus in hot spot D the radio-brightest region seems to be where the high-energy electrons radiating at 230 GHz are more concentrated, and so where the radio spectrum is flattest. On the other hand, the low-energy electrons responsible for scattering microwave photons up to X-ray energies are widely distributed, extending, for example, into the tail region in hot spot D.

Figures 8 and 9 show significant X-ray bridges between hot spots A and B, and hot spots D and E, which follow the 230 GHz extensions and so correspond to regions of flatter radio emission. This may imply either that there is fast electron streaming (at $\sim 0.5c$) in this region from acceleration sites in the hot spots, or that there is local reacceleration of both the 1-GeV electrons that up-scatter radio photons to X-ray energies and the higher-energy electrons that radiate at 230 GHz.

The inverse-Compton argument for the magnetic field strength in hot spots A, B, and D is weakened if the hot spots are taken to be non-static. A velocity $\sim 0.5c$ for hot spot B (and a lower field) could allow the emission to be inverse-Compton scattering off the microwave background radiation, rather than off its synchrotron radiation, and could produce the compression ahead of the hot spot required to explain the strong rotation measure feature reported by Carilli et al. (1988). While such high velocities have generally been ruled out for the brightest hot spots on the grounds of their side-to-side symmetry, this is not necessarily a strong argument against relativistic motions of smaller hot spots, like hot spot B.

An alternative explanation for the X-ray emission from the hot spots might be that they are synchrotron emission, but the flatness of the X-ray emission relative to the steeper spectrum of the high-frequency radio emission is then unexpected, and the electron energy spectrum must flatten substantially at high energies.

5. SUMMARY

1. Spectral index gradients as large as 0.1 arcsec^{-1} are seen in the hot spots, with the flattest spectra being seen at the peaks of compact hot spots B and E, and in the extended regions between these hot spots and the brighter extended hot spots A and D.

2. The relatively straight hot spot spectra suggest that continuous injection of relativistic electrons is occurring on time scales of 50,000 years or less.

3. The images of the hot spots in Cygnus A show that the angular size decreases from 5 to 230 GHz, consistent with electrons with energies $\gtrsim$ 10 GeV lying in a smaller region than electrons with energies $\lesssim$ 1 GeV.

4. The X-ray emission is a closer match to the angular size of the hot spots at lower frequencies, consistent with an inverse Compton interpretation of the X-radiation and magnetic fields $\sim$ 20 nT.

5. The X-ray spectra of the hot spots are flatter than the low-frequency radio spectra, suggesting that the energy spectrum of the electrons which up-scatter photons to the X-ray waveband flattens at energies below 1 GeV.

This work was supported in part by NSF Grant AST 0228963 to the University of California. We thank C. Carilli for providing VLA Cygnus A images in digital format.

REFERENCES

Carilli, C.L., 1989, PhD thesis, MIT.
Carilli, C.L., Kurk, J.D., van der Werf, P.P., Perley, R.A., & Miley, G.K., 1999, AJ 118, 2581
Carilli, C.L., Perley, R.A., Dreher, J.W., & Leahy, J.P., 1991, ApJ 383, 554
Carilli, C.L., Perley, R.A., & Harris, D.H., 1994, MNRAS 270, 173
Carilli, C.L., Perley, R.A., & Dreher, J.W. 1988, ApJ 334, L73
Hardcastle, M.J., Birkinshaw, M., Cameron, R.A., Harris, D.E., Looney, L.W., Worrall, D.M., 2002, ApJ 581, 948
Harris, D.E., Carilli, C.L., Perley, R.A., 1994, Nature 367, 713
Owen, F.N., Ledlow, M.J., Morrison, G.E. & Hill, J.M., 1997, ApJ 488, L15
Sault, R.J., Teuben, P.J., & Wright, M.C.H., 1995, in Astronomical Data Analysis Software and Systems IV, ed. R. Shaw, H.E. Payne, & J.J.E.Hayes, ASP Conf. Ser. 77, 433
Tregillis, I.L., Jones, T.W., Ryu, D., 2002. ApJ, in press (astro-ph/0310719)
Welch, W.J., Thornton, D.D., Plambeck, R.L., Wright, M.C.H., et al., 1996, PASP 108, 93
Wilson, A.S., Young, A.J. & Shopbell, P.L., 2000, ApJ 544, L27
Wright, M.C.H. & Birkinshaw, M., 1984, ApJ 281, 135
Wright, M.C.H., Chernin, L.M., Forster, J.R., 1997, ApJ 483, 783
Wright, M.C.H. & Sault, R.J., 1993, ApJ 402, 546

Table 1
Size of Cygnus A hot spots versus frequency

	Frequency (GHz)	Peak (Jy/counts)	Total (Jy/counts)	FWHM (arcsec)	Deconvolved (arcsec)
A	X-ray	83.5	486.8	2.63×1.86	2.46×1.64
	230	0.177	0.43	2.65×2.11	2.08×1.58
	87	0.308	1.49	2.42×1.68	2.22×1.43
	15	2.00	10.80	2.45×1.85	2.25×1.63
	5	7.58	44.60	2.51×1.98	2.32×1.77
B	X-ray	30.6	139.2	2.16×1.78	1.93×1.55
	230	0.054	0.110	1.32×1.29	0.99×0.86
	87	0.204	0.436	1.51×1.18	1.19×0.77
	15	0.932	2.47	1.68×1.32	1.37×0.99
	5	2.94	9.96	1.79×1.59	1.50×1.33
nucleus	X-ray	1474.	3836.0	1.53×1.43	1.21×1.10
	230	0.39	0.48	1.10×0.91	0.56×0.27
	87	0.98	1.05	1.02×0.88	0.29×0.19
	15	1.27	1.35	1.02×0.88	0.29×0.16
	5	0.82	0.88	1.02×0.89	0.35×0.12
D	X-ray	134.9	683.3	2.21×1.93	2.02×1.68
	230	0.20	0.87	2.23×1.66	2.05×1.36
	87	0.65	2.49	2.02×1.59	1.81×1.27
	15	3.97	17.74	2.16×1.74	1.96×1.47
	5	12.28	57.69	2.20×1.81	1.99×1.55
E	X-ray	10.64	65.81	2.51×2.07	2.32×1.87
	230	0.053	0.10	2.88×1.48	2.40×0.44
	87	0.099	0.19	1.51×1.08	1.17×0.61
	15	0.476	1.16	1.87×1.11	1.59×0.69
	5	1.291	3.90	2.14×1.19	1.90×0.82

1. The X-ray entries are $0.5-7.5$ keV fluxes, rather than flux densities, and are in *Chandra* ACIS counts.
2. The radio flux densities have a $\sim 10\%$ absolute calibration error. The errors for the Gaussian fits depend on the SNR and on the atmospheric decorrelation at 87 and 230 GHz, and for hot spots A, B, and D were empirically measured to be $0.01-0.02''$ at 5 and 15 GHz, and $0.04-0.10''$ at 87 and 230 GHz. The size of hot spot E is poorly determined ($\sim 0.5''$ at 230 GHz). The deconvolved size of the nucleus results from calibration errors and atmospheric coherence at 230 GHz. The values given for the FWHM have not been corrected for this instrumental and atmospheric "seeing."

Table 2
Fitted X-ray parameters and implied magnetic field

	α_5^{230}	α_X	$S_{1\,\mathrm{keV}}$ (nJy)	$N_{\mathrm{H,int}}$ (10^{21} cm^{-2})	energy range (keV)	B_{eq} (nT)	B_{fit} (nT)
A	1.40 ± 0.05	0.64 ± 0.07	26.7 ± 1.6	$0^{(1)}$	$0.5-7.5$	21	12
		0.77 ± 0.13	31.2 ± 4.3	3.6 ± 0.5			11
B	1.15 ± 0.05	0.50 ± 0.17	5.3 ± 0.7	$0^{(1)}$	$0.5-4.5$	24	12
		0.70 ± 0.35	6.8 ± 2.6	4.0 ± 1.5			10
D	1.05 ± 0.05	0.61 ± 0.06	38.1 ± 2.0	$0^{(1)}$	$0.5-6.0$	27	19
		0.80 ± 0.11	47.9 ± 5.9	3.9 ± 0.4			18

$^{(1)}$ Zero intrinsic N_{H} assumed.

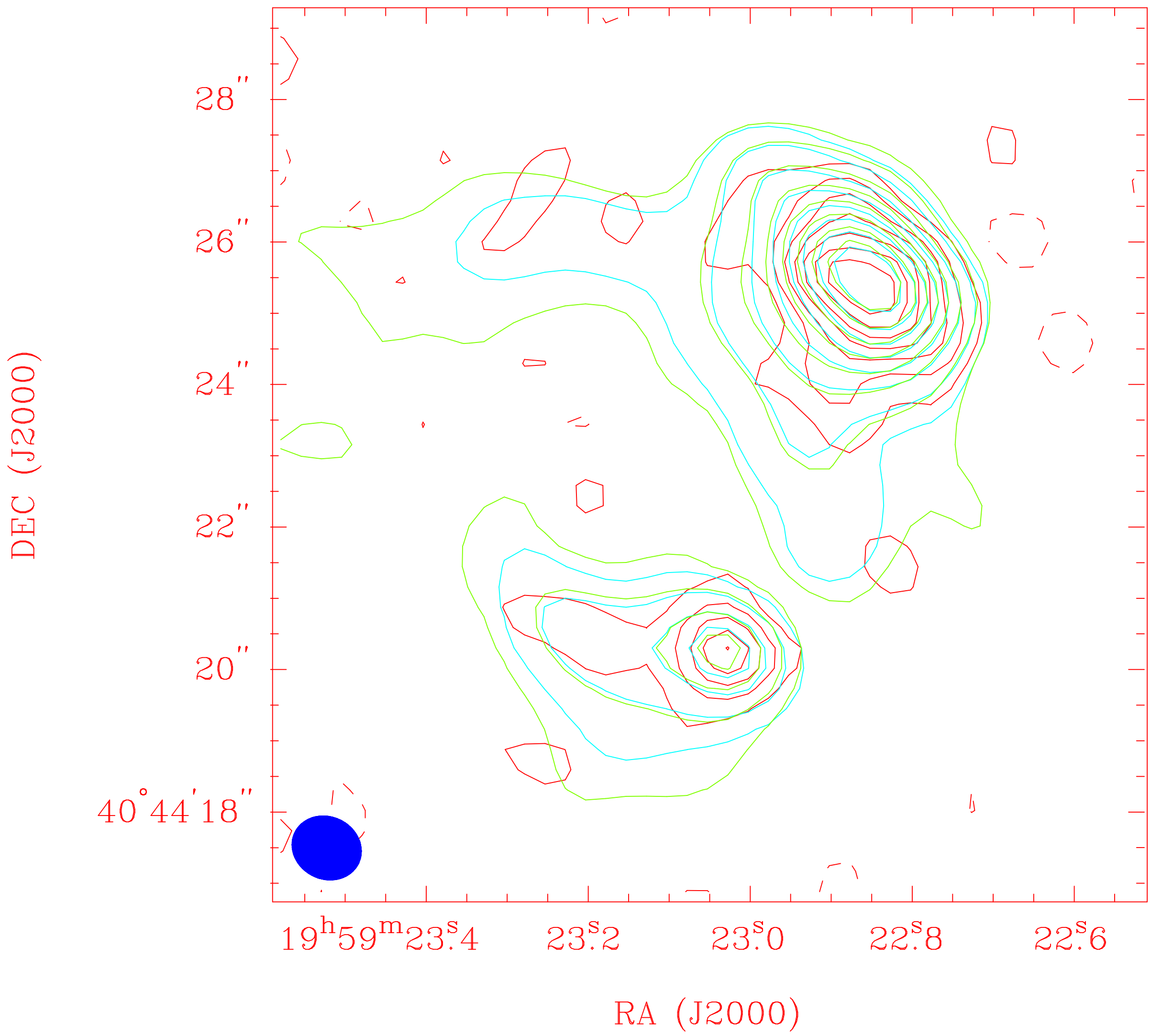

FIG. 1.— Hot spots A and B. Contours of emission at 230 GHz (red) 15 GHz (blue) and 5 GHz (green). Contours at intervals of 12.5% × peak brightness 0.096, 2.08 and 7.85 Jy/beam; additional 6.25% contour at 5 and 15 GHz. The beam FWHM is indicated in lower left. The 12.5% contour is 12 mJy/beam (1.7× RMS) at 230 GHz.

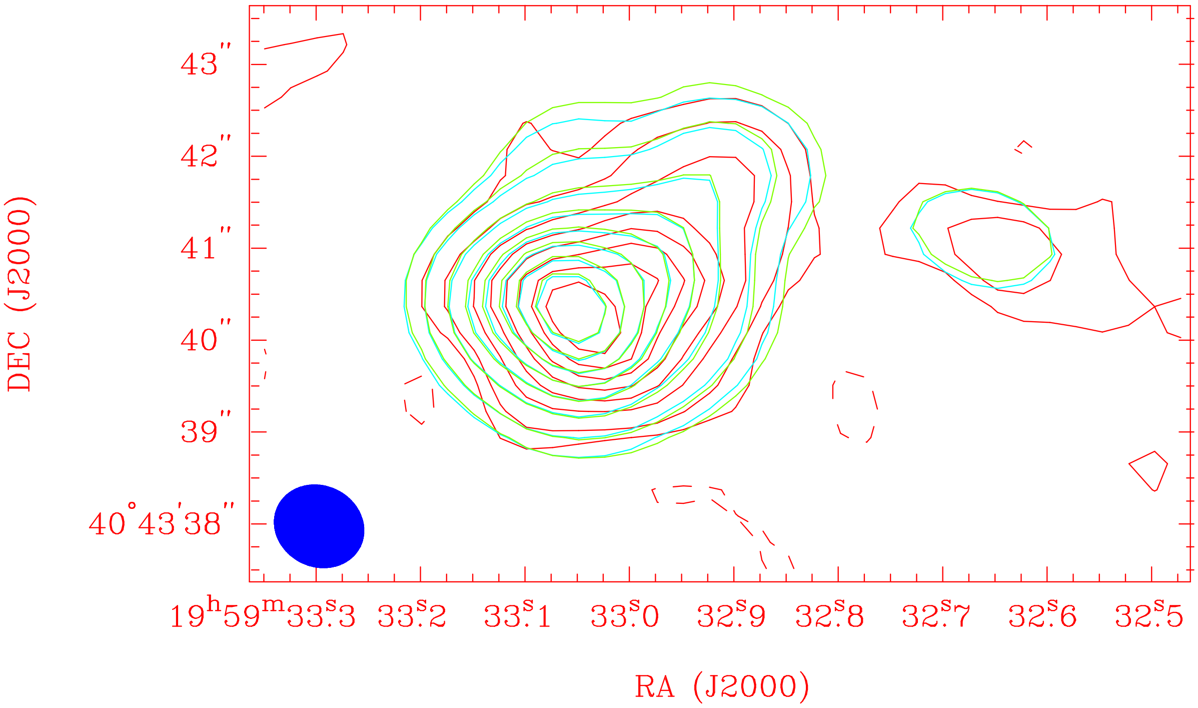

FIG. 2.— Hot spots D and E. Contours of emission at 230 GHz (red) 15 GHz (blue) and 5 GHz (green). Contours at intervals of 12.5% × peak brightness 0.20, 4.19 and 13.0 Jy/beam; additional 6.25% contour. The beam FWHM is indicated in lower left. The 6.25% contour is 13 mJy/beam (1.7× RMS) at 230 GHz.

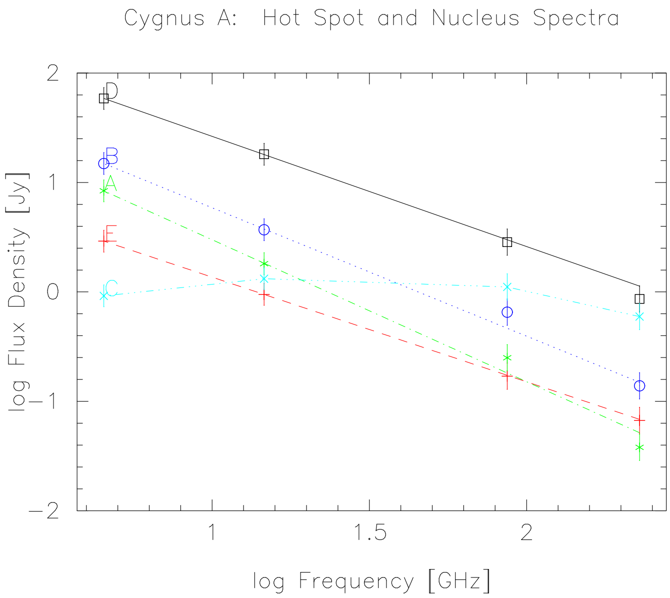

FIG. 3.— Spectra for hot spots A, B, D, E, and the nucleus of Cygnus A, from 5 to 230 GHz. We used 10% calibration error bars at 5 and 15 GHz and 12% at 87 and 230 GHz. The straight lines show the best fit spectral index to each of the hot spots.

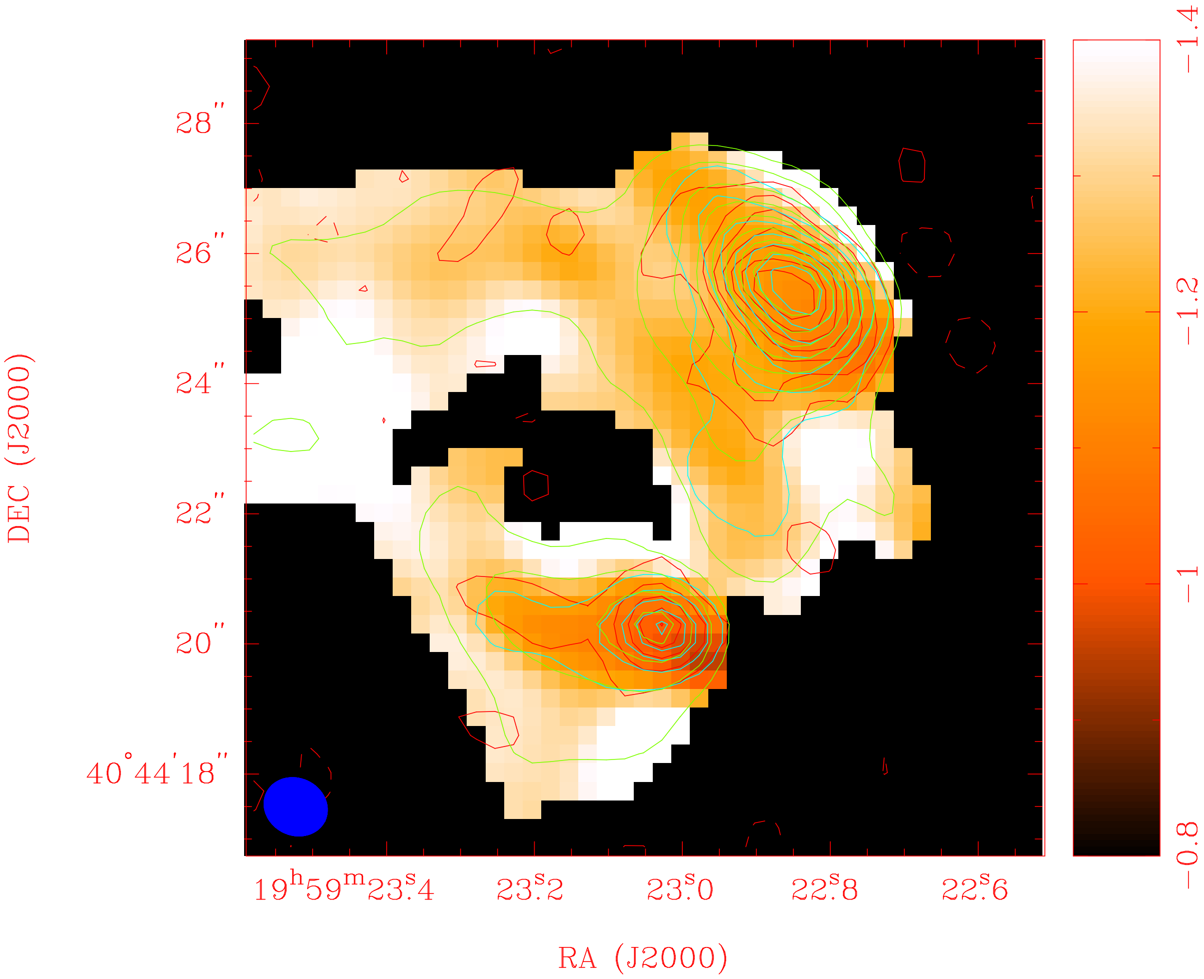

FIG. 4.— Hot Spots A and B. Contours of emission at 230 GHz (red) 87 GHz (blue) and 5 GHz (green), superposed on spectral index image from 5 to 15 GHz. Contours at intervals of 12.5% × peak brightness 0.096, 0.34 and 7.85 Jy/beam; additional 6.25% contour at 5 GHz. The beam FWHM is indicated in lower left.

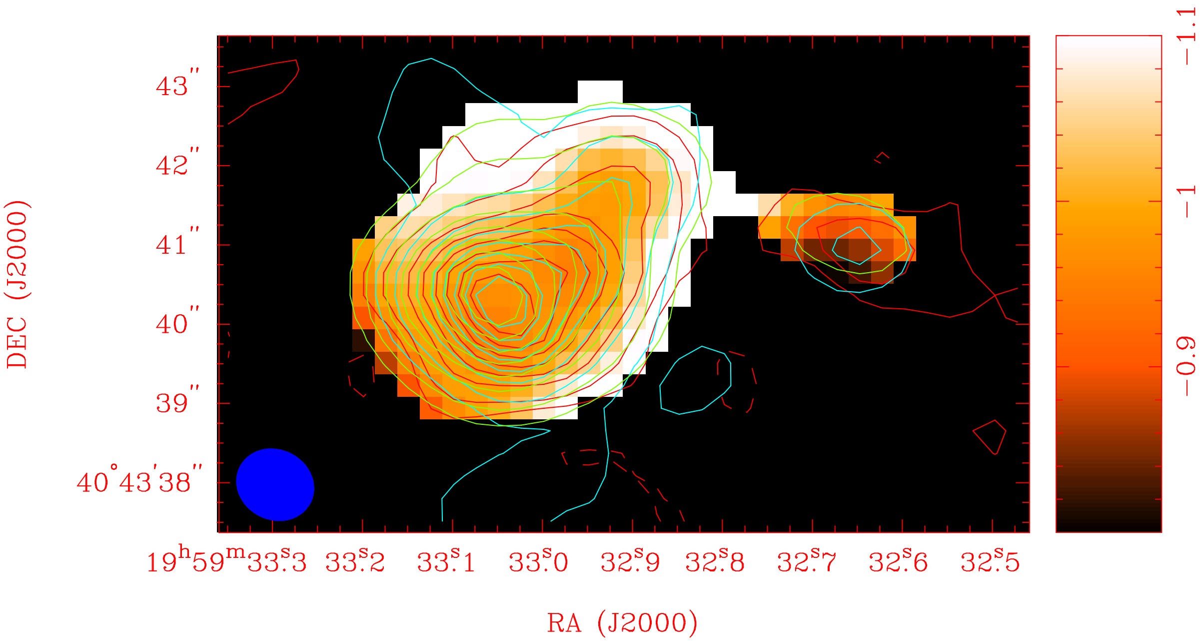

FIG. 5.— Hot spots D and E. Contours of emission at 230 GHz (red) 87 GHz (blue) and 5 GHz (green), superposed on spectral index image from 5 to 15 GHz. Contours at intervals of 12.5% × peak brightness 0.20, 0.73 and 13.0 Jy/beam; additional 6.25% contour. The beam FWHM is indicated in lower left.

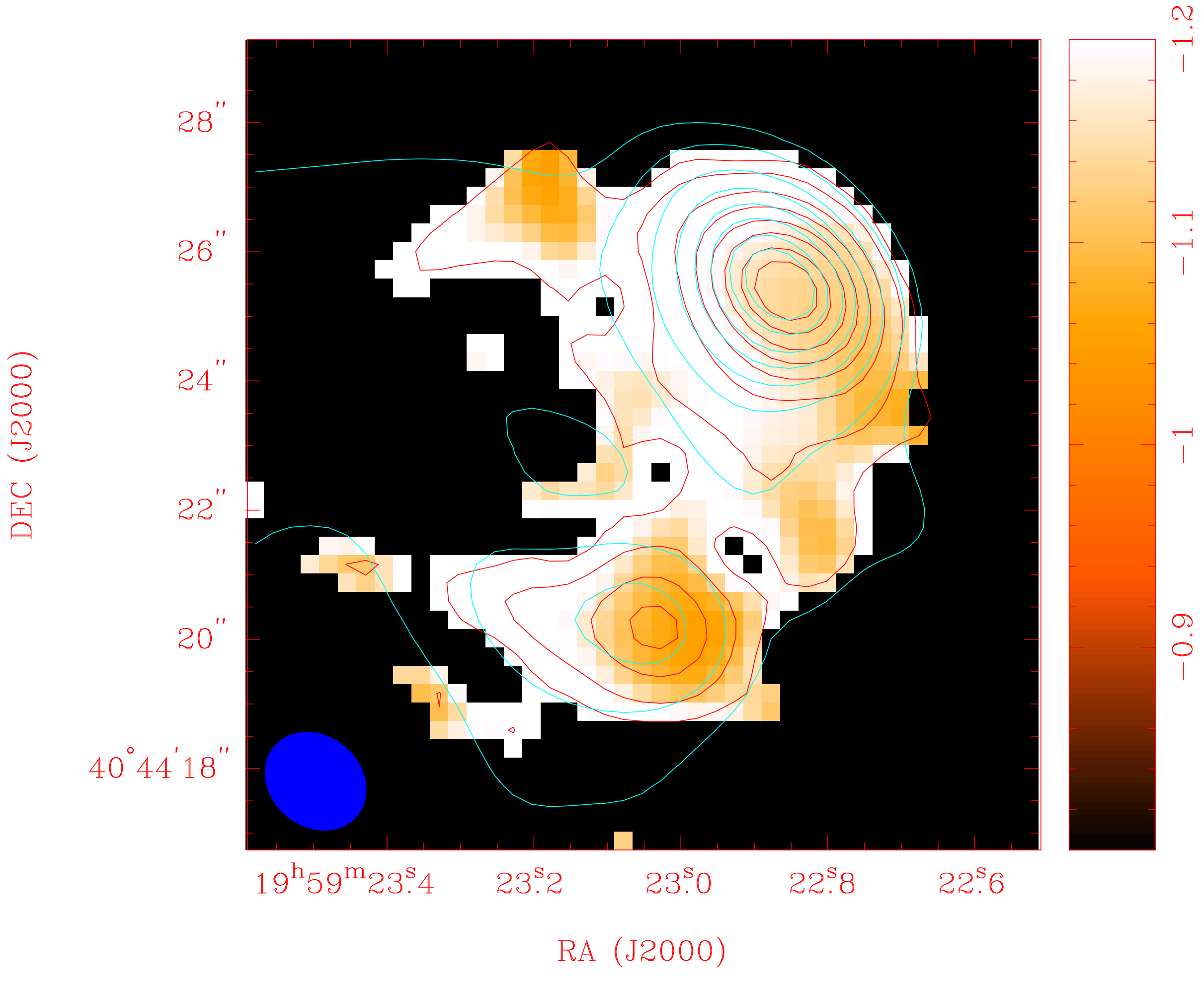

FIG. 6.— Hot Spots A and B. Contours of emission at 230 GHz (red) 5 GHz (blue), superposed on spectral index image from 5 to 230 GHz at 1.65″ × 1.38″ resolution. Contours at intervals of 12.5% × peak brightness 0.19 and 16.07 Jy/beam; additional 6.25% contour at 5 and 230 GHz. The beam FWHM is indicated in lower left.

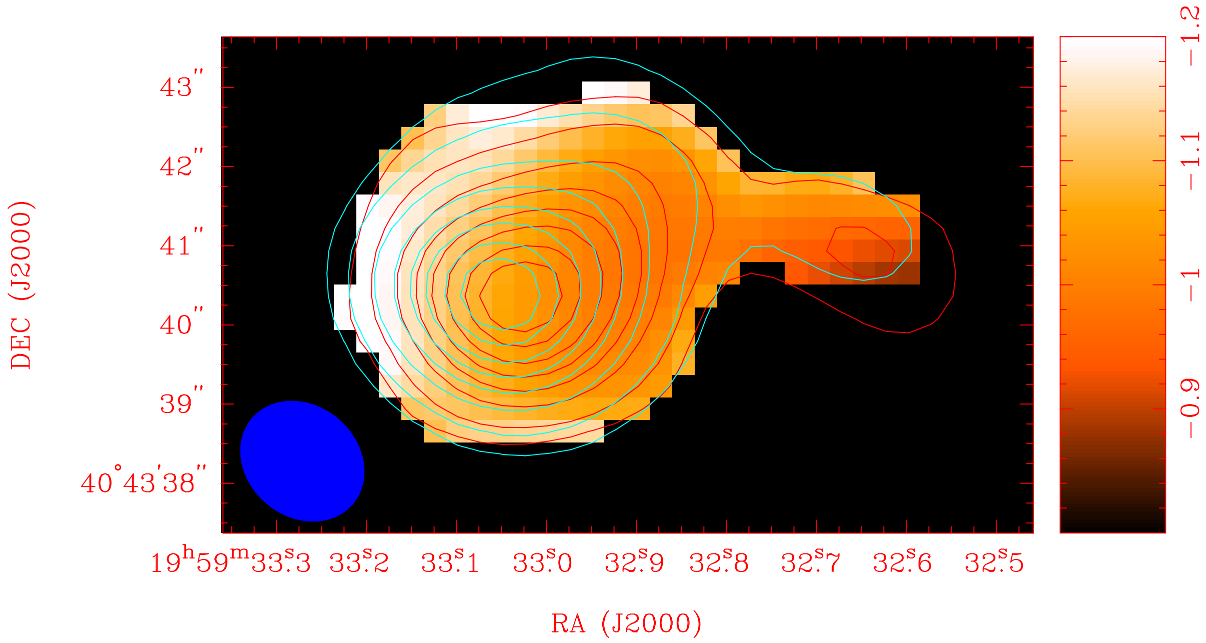

FIG. 7.— Hot Spots D and E. Contours of emission at 230 GHz (red) 5 GHz (blue), superposed on spectral index image from 5 to 230 GHz at $1.65'' \times 1.38''$ resolution. Contours at intervals of 12.5% × peak brightness 0.39 and 24.47 Jy/beam; additional 6.25% contour at 5 and 230 GHz. The beam FWHM is indicated in lower left.

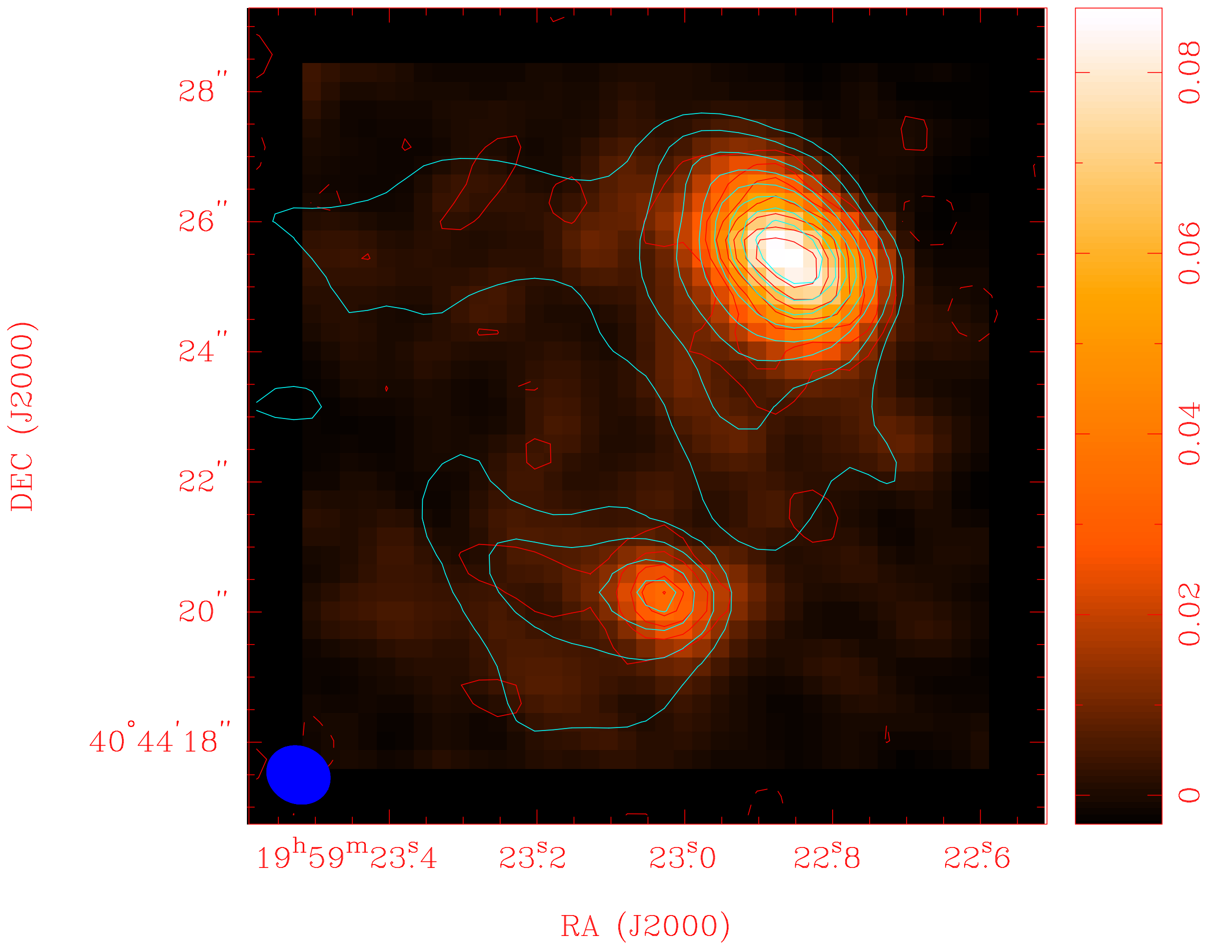

FIG. 8.— Hot spots A and B. Contours of emission at 230 GHz (red) and 5 GHz (blue) superposed on *Chandra 0.5 - 8.0 keV X-ray image.* Contours at intervals of 12.5% × peak brightness 0.096 and 7.85 Jy/beam; additional 6.25% contour at 5 GHz. The overall extent of the X-ray emission more closely resembles the synchrotron emission at 5 GHz than at 230 GHz. The beam FWHM is indicated in lower left.

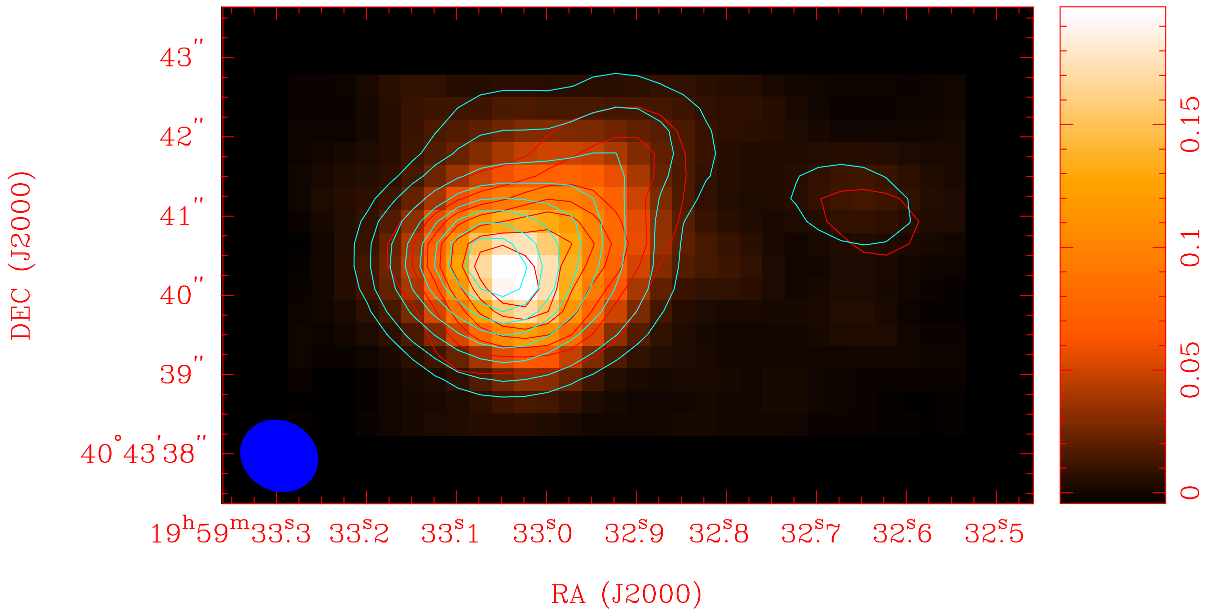

FIG. 9.— Hot Spots D and E. Contours of emission at 230 GHz (red) and 5 GHz (blue) superposed on *Chandra* 0.5 - 8.0 keV X-ray image. Contours at intervals of 12.5% × peak brightness 0.20 and 13.0 Jy/beam; additional 6.25% contour at 5 GHz. The beam FWHM is indicated in lower left.